Monthly Notices
of the
ROYAL ASTRONOMICAL SOCIETY

Mon. Not. R. Astron. Soc. **399,** 1681–1693 (2009) doi:10.1111/j.1365-2966.2009.15420.x

Statistical assessment of shapes and magnetic field orientations in molecular clouds through polarization observations

K. Tassis,[1⋆] C. D. Dowell,[1] R. H. Hildebrand,[2,3] L. Kirby[2] and J. E. Vaillancourt[4]

[1]*Jet Propulsion Laboratory, California Institute of Technology, Pasadena, CA 91109, USA*
[2]*Enrico Fermi Institute and Department of Astronomy and Astrophysics, University of Chicago, 5640 South Ellis Avenue, Chicago, IL 60637, USA*
[3]*Department of Physics, University of Chicago, 5720 S. Ellis Ave. Chicago, IL 60637, USA*
[4]*Division of Physics, Mathematics, & Astronomy, California Institute of Technology, Pasadena, CA 91125, USA*

Accepted 2009 July 8. Received 2009 June 15; in original form 2009 April 3

ABSTRACT

We present a novel statistical analysis aimed at deriving the intrinsic shapes and magnetic field orientations of molecular clouds using dust emission and polarization observations by the Hertz polarimeter. Our observables are the aspect ratio of the projected plane-of-the-sky cloud image and the angle between the mean direction of the plane-of-the-sky component of the magnetic field and the short axis of the cloud image. To overcome projection effects due to the unknown orientation of the line-of-sight, we combine observations from 24 clouds, assuming that line-of-sight orientations are random and all are equally probable. Through a weighted least-squares analysis, we find that the best-fitting intrinsic cloud shape describing our sample is an oblate disc with only small degrees of triaxiality. The best-fitting intrinsic magnetic field orientation is close to the direction of the shortest cloud axis, with small ($\sim$24°) deviations towards the long/middle cloud axes. However, due to the small number of observed clouds, the power of our analysis to reject alternative configurations is limited.

Key words: magnetic fields – methods: statistical – techniques: polarimetric – ISM: clouds.

1 INTRODUCTION

Far-infrared and submillimetre emission from molecular clouds appears polarized, presumably as a result of the alignment of elongated dust grains with the cloud magnetic field (see e.g. Dotson et al. 2000, 2009; Hildebrand et al. 2000; Lazarian 2003, 2007; Curran & Chrysostomou 2007; Hoang & Lazarian 2008). Measurable degrees of polarization, at the few per cent level, are typical in many interstellar clouds and cloud cores (Dotson et al. 2000, 2009). Additionally, theoretical advancements in understanding grain alignment (e.g. Bethell et al. 2007) indicate that even in relatively dense clouds, dust polarization traces the underlying magnetic field structure. The ubiquity of magnetic fields and dust in the interstellar medium makes polarization observations a powerful tool for distinguishing between theories of molecular cloud formation, support and evolution.

From a theoretical point of view, the orientation of the mean magnetic field in molecular clouds is closely tied to the dynamical importance of magnetic forces compared to gravity, random motions (turbulence) and thermal pressure. If magnetic fields are dynamically important, and are responsible for a significant fraction of the support of molecular clouds against gravity, then the mean magnetic field is preferentially oriented parallel to the shortest axis of the molecular cloud (e.g. Mouschovias 1978). This is a result of an increased support against gravity in the direction perpendicular to the magnetic field compared to the direction parallel to it. The cloud contracts more in the direction parallel to the magnetic field than in the direction perpendicular to the field. An additional result of magnetic support is that the intrinsic shapes of molecular clouds in this case resemble mostly oblate (although not necessarily axisymmetric), flattened ellipsoids (one axis appreciably smaller than the other two).

If magnetic fields are dynamically unimportant compared to turbulence, then turbulent motions dominate the internal dynamics of clouds, and the magnetic fields are dragged around by turbulent eddies (e.g. Ballesteros-Paredes, Vázquez-Semadeni & Scalo 1999). In this case, the mean magnetic field has a random orientation with respect to the molecular cloud principal axes. The shape distribution for overdensities formed in a turbulent field is also random (Gammie et al. 2003). Molecular clouds forming out of magnetohydrodynamic turbulence in the weak-field regime therefore would be expected to have random shapes and random magnetic field orientations.

A third possibility is that magnetic fields have a helical configuration and thread prolate (filamentary) molecular clouds (Fiege & Pudritz 2000a). The most common outcome of such configurations is polarization patterns that may contain 90° flips of the

⋆E-mail: ktassis@jpl.nasa.gov

polarization direction (Fiege & Pudritz 2000b). Additional ideas for molecular cloud shapes come from non-magnetic calculations; for example finite, self-gravitating gaseous sheets have been shown to collapse to filamentary structures with mass concentrations close to the edges or ends of the filaments (e.g. Burkert & Hartmann 2004; Hartmann & Burkert 2007).

If it were possible to determine the mean orientation of the ordered magnetic field in molecular clouds, then important constraints could be placed on theories of molecular cloud formation and support. However, such a task is not straightforward, due to various projection effects which prohibit us from knowing either the true orientation of the magnetic field or the principal axes of the cloud ellipsoid. Polarization measurements can only determine the orientation of the magnetic field on the plane-of-the-sky (POS), and, similarly, only the shape of the POS projection of the cloud can be measured. As a result, the magnetic field may be oriented, for example, along the shortest cloud axis, but its projection on the sky may appear closest to the major axis of the projected cloud ellipse. These difficulties were explicitly demonstrated by Basu (2000).

An effective way to overcome these difficulties and use polarization measurements to constrain theoretical models for the orientation of the mean magnetic field in molecular clouds is through a statistical treatment. Assuming that the orientation of the clouds themselves with respect to our line-of-sight (LOS) is random, we can assess the likelihood of different underlying distributions of molecular cloud shapes, and of orientations of the mean magnetic field in molecular clouds. In this work, we present a new method for such a treatment. We study a sample of 24 molecular clouds with measured apparent elongations and field orientations. By applying a weighted least-squares analysis, we derive the most probable intrinsic shapes and most probable magnetic field orientations for the parent population that the 24 clouds sample.

This paper is organized as follows. The observations and analysis used to derive elongations and apparent field orientations in the sample clouds are described in Section 2. The formalism used in our analysis, including a short discussion of projection effects and a description of our statistical analysis, is discussed in Section 3 (a detailed mathematical treatment of projection effects and the statistical analysis are given in Appendices A and B, respectively). Our results are presented in Section 4, and discussed in Section 5.

2 OBSERVATIONS

The Hertz polarimeter (Schleuning et al. 1997; Dowell et al. 1998) deployed at the Caltech Submillimetre Observatory has been used to map the flux density and polarization of molecular clouds on scales of several arcmin at a wavelength of 350 μm. In a complete sample of 56 Galactic clouds, 32 contain two or more polarization measurements satisfying the criterion $P \geq 3\sigma_{\rm p}$ or better, where P is the measured polarization amplitude and $\sigma_{\rm p}$ is its measurement uncertainty.[1] The clouds are listed in Table 1; object positions and complete maps of flux density and polarization can be found in Dotson et al. (2009).

[1]In counting 32 clouds, we have counted separately two components of OMC-3 with distinct cores separated by more than 2 arcmin, with no Hertz measurement of flux in between.

2.1 Polarization

Within each cloud, we limit the data points used to calculate mean polarizations to those satisfying the condition $P \geq 3\sigma_{\rm p}$. The best estimate of the POS-projected magnetic field direction is that of the measured polarization vector (rotated by 90°). The amplitude of the polarization P yields some information about the inclination of the field to the LOS. However, P is also dependent on a number of other factors which are independent of the field, including the dust grain shape and alignment efficiency, and the magnetic field structure along the LOS and within the telescope beam (e.g. Draine & Lee 1985). Therefore, our analysis of the magnetic field will involve only the polarization position angle.

The mean polarization position angle $\langle\chi\rangle$ is defined by averaging Stokes parameters of unit magnitude such that

$$\langle\chi\rangle \equiv \frac{1}{2}\tan^{-1}\frac{\langle\sin 2\chi\rangle}{\langle\cos 2\chi\rangle}, \tag{1}$$

where

$$\langle\sin 2\chi\rangle = \frac{1}{N}\sum_{i=1}^{N}\sin 2\chi_i, \tag{2}$$

$$\langle\cos 2\chi\rangle = \frac{1}{N}\sum_{i=1}^{N}\cos 2\chi_i, \tag{3}$$

and the χ_is are the measured polarization angles at each position i in the cloud. The sums are over all N points in the map where the measured polarization $P \geq 3\sigma_{\rm p}$.

We calculate the standard deviation of the mean $\langle\chi\rangle$ under the assumption of zero intrinsic dispersion (i.e. under the assumption that all of the dispersion in the observed χ_i is due to observational errors) as

$$\sigma_{\langle\chi\rangle} = \frac{1}{N}\left[\sum_{i=1}^{N}\sigma_i^2\right]^{1/2}, \tag{4}$$

where the σ_i are the uncertainties on the measurements of χ_i. The measurement accuracy is limited by Hertz's systematic uncertainties such that $\sigma_{\langle\chi\rangle} \geq 2°$ (Dowell et al. 1998). In our case, the dispersion in the observed values of χ_i in individual clouds is substantial, so we also calculate the dispersion about the mean, σ_χ, given by the standard deviation of the measurements

$$\sigma_\chi = \left[\frac{1}{N-1}\sum_{i=1}^{N}(\chi_i - \langle\chi\rangle)^2\right]^{1/2}. \tag{5}$$

In using this equation we have accounted for the 180° periodicity in the polarization angles.

Each cloud's mean polarization amplitude is given by

$$\langle P\rangle \equiv \frac{\sqrt{\langle Q\rangle^2 + \langle U\rangle^2}}{\langle I\rangle} \tag{6}$$

where I, Q and U are the measured Stokes parameters. The mean polarizations, angles and uncertainties are all reported in Table 1. The $\langle P\rangle$s reported in Table 1 have been de-biased using the statistical measurement uncertainty on the mean (e.g. Vaillancourt 2006). However, the measurement uncertainties in the table are not those used to de-bias, but are at least as large as Hertz's systematic uncertainties such that $\sigma_{\langle p\rangle} \geq 0.2$ per cent (Dowell et al. 1998).

Table 1. Mean polarization and cloud shape parameters.

Object no.	Object[b] name	No. vectors	Mean polarization parameters (E-vector)[a] $\langle P \rangle$ (per cent)	$\sigma_{\langle p \rangle}$ (per cent)	$\langle \chi \rangle$ (°)	$\sigma_{\langle \chi \rangle}$ (°)	σ_χ[c] (°)	Cloud shape Aspect ratio	Angle[d] (°)	$\lvert\lambda\rvert$[e] (°)
1	W3[h]	51	0.6	0.2	65	2	32	0.83	−80	35
2	NGC 1333	18	1.6	0.2	88	2	19	0.68	−45	48
3	IRAS 05327−0457	18	3.9	0.4	−40	2	17	0.92	−37	3
4	OMC-1	437	2.0	0.2	25	2	26	0.51	5	20
5	OMC-2[h]	26	0.7	0.2	−39	4	33	0.44	14	53
6	OMC-3 MMS 6[f]	43	2.1	0.2	−42	2	12	0.74	−51	9
7	OMC-3 MMS 9[f]	21	1.2	0.2	−62	2	20	0.95	11	73
8	OMC-4	16	1.7	0.2	−14	2	13	0.84	57	71
9	NGC 2024	54	0.7	0.2	−23	2	24	0.65	−15	8
10	NCG 2068 LBS17	3	8.3	1.5	81	5	16	0.98	−50	49
11	NCG 2068 LBS10	43	3.8	0.2	−51	2	20	0.93	38	89
12	NGC 2071	6	0.6	0.2	−27	4	25	0.97	−13	14
13	Mon R2[h]	49	0.7	0.2	31	2	32	0.82	47	16
14	GGD12	17	1.2	0.2	89	2	16	0.94	−60	31
15	S269	7	2.9	0.3	30	3	13	0.82	−18	48
16	AFGL 961[h]	5	1.9	0.7	−10	4	44	0.86	−37	27
17	Mon OB1 12[g]	26	2.0	0.2	−37	2	17	0.76	27	64
18	NGC 2264	18	0.6	0.2	77	2	16	0.84	−47	56
19	ρ Oph	41	1.6	0.2	−21	2	13	0.76	7	29
20	IRAS 16293	7	0.6	0.2	90	3	25	0.67	−65	26
21	NGC 6334 V[h]	8	0.3	0.2	90	3	34	0.93	−53	37
22	NGC 6334 A	49	1.3	0.2	69	2	18	0.89	−3	71
23	NGC 6334 I	54	0.9	0.2	41	2	19	0.51	11	30
24	W33 C[h]	29	0.4	0.2	48	2	37	0.88	82	35
25	W33 A	19	0.9	0.2	−53	2	13	0.90	−49	4
26	M17	127	0.9	0.2	−13	2	27	0.59	−10	3
27	W43-MM1	4	1.5	0.3	9	4	22	0.88	34	25
28	G34[h]	44	0.5	0.2	−66	2	41	0.94	72	42
29	W49 A	32	0.6	0.2	59	2	29	0.87	−80	41
30	W51 A	109	0.5	0.2	44	2	28	0.71	−78	58
31	W75 N[h]	9	0.3	0.2	44	3	47	0.98	76	33
32	DR21	142	1.2	0.2	5	2	20	0.26	0	5

[a]Mean polarization parameters defined in equations (1)–(6). Means are calculated using only the $P \geq 3\sigma_p$ vectors shown in 'No. vectors' column. Angle χ is measured east of north.
[b]Object names follow the convention in Dotson et al. (2009); list is ordered with approximately increasing right ascension.
[c]Dispersion about mean polarization angle given by equation (5).
[d]Direction of long cloud axis, measured east of north.
[e]Angle between mean polarization angle and long cloud axis. This is equivalent to the angle between the inferred magnetic field direction and the short cloud axis.
[f]Part of OMC-3 in Dotson et al. (2009).
[g]a.k.a. IRAS 06382+0939.
[h]Objects with angle dispersion larger than 30° are not included in the angle analysis.

2.2 Cloud shapes

In the case of a symmetric ellipsoidal cloud, the first and second moments of the flux density describe the cloud's centre and width. The location of the cloud's centre (x_0, y_0) is given by the first moments:

$$x_0 = \frac{\sum_i x_i \; F(x_i, y_i)}{\sum_i F(x_i, y_i)}, \tag{7}$$

$$y_0 = \frac{\sum_i y_i \; F(x_i, y_i)}{\sum_i F(x_i, y_i)}. \tag{8}$$

where the sum is over all points i in the flux density map. No cuts are applied to the flux density data beyond those already made in the Dotson et al. (2009) archive. (The $P \geq 3\sigma_p$ criterion is not applied.)

The second moments compose the three elements of a symmetric 2×2 matrix

$$\mathbf{I} = \begin{pmatrix} I_{xx} & I_{xy} \\ I_{xy} & I_{yy} \end{pmatrix} \tag{9}$$

with elements

$$I_{xx} = \sum_i (y_i - y_0)^2 \; F(x_i, y_i), \tag{10}$$

$$I_{xy} = -\sum_i (x_i - x_0)(y_i - y_0) \; F(x_i, y_i), \tag{11}$$

$$I_{yy} = \sum_i (x_i - x_0)^2 \; F(x_i, y_i). \tag{12}$$

The principal moments of the cloud are simply the eigenvalues, I_1 and I_2, of $\mathbf{I}$. Defining $I_1 \geq I_2$, the aspect ratio is given by $q = \sqrt{I_2/I_1}$ and the position angle of the long cloud axis is determined from the eigenvector corresponding to the eigenvalue I_2.

The first and second moments are well defined and express the distribution of the flux density in the cloud even when the shape is irregular and cannot be well approximated by an ellipse. Therefore, we use these moments to define the aspect ratio and position angle of the principal axes for all clouds in our sample, with the caveat that we have ignored any higher-order moments which more precisely characterize the cloud shape. We note that some bias can be introduced through the finite size of each map.

Examples of the mean polarization and cloud shape calculations are shown in Fig. 1 for the most elongated cloud, and Fig. 2 for a nearly circular cloud. The measured cloud parameters are given in Table 1. The apparent cloud aspect ratio q and the absolute value of the angle between mean field and short apparent axis, λ, are plotted in Fig. 3. Data shown as open circles in Fig. 3 and denoted by *h* in Table 1 are not included in further analysis due to their large ($>30^\circ$) dispersion in λ.

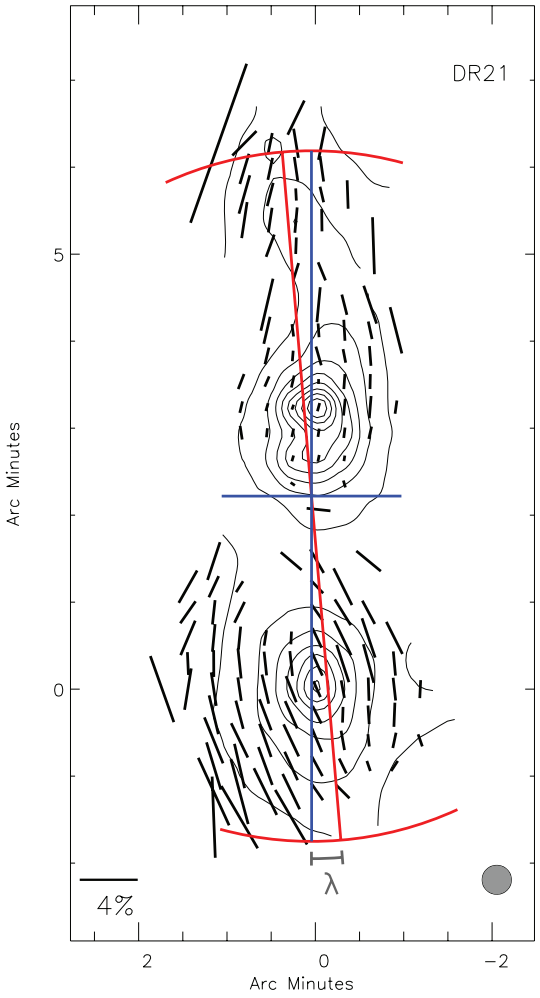

Figure 1. Mean polarization and cloud shape in DR21. Polarization measurements (small black line segments) are plotted with their lengths proportional to P (scale at lower left); only $P \geq 3\sigma_p$ measurements are shown. The mean polarization direction (E-vector) and its dispersion are shown as the red line and the arcs at its end. The cloud principal axes are drawn as blue lines; their relative lengths are given by the aspect ratio $q = 0.26$. The lines corresponding to the mean polarization and cloud widths intersect at the cloud centre (x_0, y_0) and are drawn with arbitrary absolute lengths. The grey arc labelled 'λ' denotes the difference between the mean polarization angle and the cloud position angle. Coordinate offsets from $20^h39^m1\overset{s}{.}1, 42^\circ19'31''$ (J2000). Contours are 10, 20, ... , 90 per cent of the peak flux density of 820 Jy beam^{-1} [at $(\Delta\alpha, \Delta\delta) = (0', 3\overset{'}{.}3)$]. The shaded circle at lower right is the 20 arcsec FWHM Hertz beam.

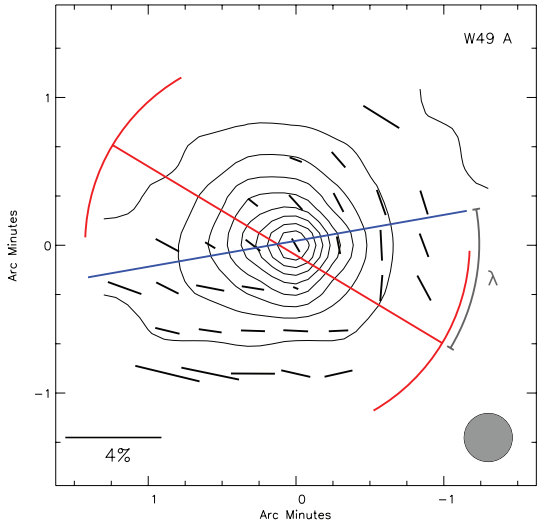

Figure 2. Same as Fig. 1 but for the cloud W49 A. As this cloud is nearly circular (aspect ratio $q = 0.87$) we plot only the long cloud principal axis for clarity. Coordinate offsets are from $19^h10^m13\overset{s}{.}6, 9^\circ6'17''$ (J2000). Contours are 10, 20, ... , 90 per cent of the peak flux density of 730 Jy beam^{-1}.

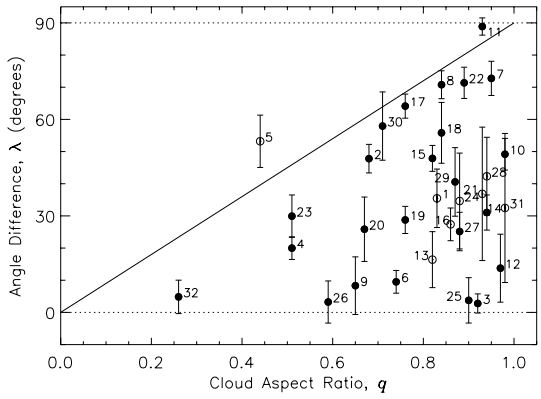

Figure 3. Aspect ratios and angles between the magnetic field and the minor cloud axis for the 32 clouds in our sample. Note that the aspect ratio q is defined so that a very elongated cloud corresponds to $q \to 0$ and a circular cloud to $q = 1$. For angles, $\lambda = 0$ corresponds to a projected magnetic field aligned with the minor axis of the projected cloud. Each error bar represents the quadrature sum of the statistical uncertainty of the cloud's mean angle uncertainty ($\sigma_{\langle\chi\rangle}$), the systematic angle uncertainty and the systematic polarization uncertainty (see text for precise definitions of these terms). Data shown as open circles are not included in further analysis due to their large dispersion in λ (all data are given in Table 1). Dotted horizontal lines are drawn at the boundaries of the allowed range $0^\circ < \lambda < 90^\circ$. The diagonal $\lambda/90^\circ = q$ is shown as a solid line.

Error bars on λ correspond to the quadrature sum of $\sigma_{\langle\chi\rangle}$, the systematic angle uncertainty (2°; Dowell et al. 1998) and the systematic polarization uncertainty ($\Delta\chi_{\rm sys}$). We estimate the last quantity using the relation

$$\Delta\chi_{\rm sys} = \frac{90^\circ}{\pi}\frac{0.2\,\text{per cent}}{\langle P\rangle}, \qquad (13)$$

where 0.2 per cent is Hertz's systematic polarization uncertainty. We note that equation (13) assumes measurements of P and χ follow normal distributions (equivalent to the assumption $P \gg \sigma_{\rm p}$). While this is clearly not true for all measurements in Table 1, this fact has minimal effect on the apparent size of the error bars and has no effect on our subsequent analysis (as the uncertainties are not used).[2]

Furthermore, these angle uncertainty estimates do not include any uncertainties in the estimate of the cloud shape, but include only the uncertainties on the measurement of the polarization angle. A visual comparison of Figs 1 and 2 should make it apparent that the uncertainty in the cloud orientation is smallest when $q = 0$ and must increase as the cloud becomes more circular ($q = 1$). An estimate of this uncertainty for all clouds in our study is beyond the scope of this paper. Neglecting these uncertainties has no effect on our conclusions as this information is not used in our subsequent data analysis.

3 ANALYSIS

3.1 Projection effects

Let us consider a triaxial ellipsoid model molecular cloud with semi-axes $a \geq b \geq c$, and axial ratios

$$\zeta = \frac{b}{a} \tag{14}$$

(middle-to-long axis ratio) and

$$\xi = \frac{c}{a} \tag{15}$$

(short-to-long axis ratio). When observed, the image of the molecular cloud appears on the POS as an ellipse. The observable quantity related to the cloud shape is the ellipse aspect ratio, q. Let us additionally assume that the molecular cloud is threaded by a magnetic field, the mean direction of which forms a polar angle θ_B with the short axis of the cloud ellipsoid and an azimuthal angle ϕ_B with the long axis of the cloud ellipsoid (see Fig. 4). Through polarimetry observations, only the direction of the projection of the field on the POS can be measured, and the associated observable quantity is the angle λ between the projected field and the minor axis of the POS cloud ellipse.

The observables q and λ can be calculated as a function of ζ, ξ, θ_B, ϕ_B and of the orientation angles of the observer's LOS, θ and ϕ. This calculation is described in detail in Appendix A.

However, the orientation of the LOS is unknown – in the absence of biases, the LOS orientation can be treated as uniformly distributed among different directions with respect to the observer. As a result, it is not generally possible to de-project the intrinsic cloud shape and magnetic field orientation for any single object. Instead, a statistical treatment must be used: the preferred intrinsic cloud shapes and magnetic field orientations in nature can only be obtained by observing a large number of clouds, and comparing the distribution of observables with expectations based on different intrinsic shapes and field orientations. In this work, we employ such a statistical analysis described below.

[2]Further study of polarization angle uncertainties at low $P/\sigma_{\rm p}$ can be found in Naghizadeh-Khouei & Clarke (1993).

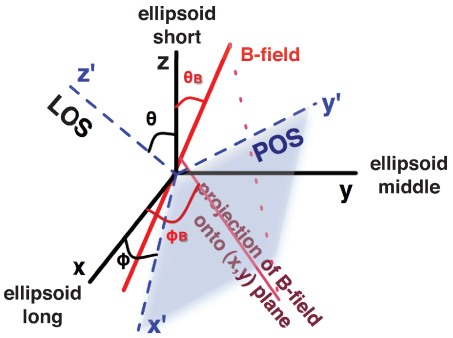

Figure 4. Solid black lines: native cloud ellipsoid coordinate system (x, y, z). Dashed blue lines: observation coordinate system (x', y', z'). The LOS is along the z' axis, and the POS is the x'– y' plane. The y' axis represents the direction of the projection of the shortest ellipsoid axis on to the POS. The directions of the magnetic field and of its projection on to the x–y plane are shown in red.

3.2 Statistical analysis

As a first proof-of-concept, we test for the presence of possible degeneracies in the distribution of the observables (q, λ) which may limit the value of this analysis. The simplest tests we can perform to verify that the data of Fig. 3 have non-trivial information content derive from the immediate observation that almost all data points lie below the diagonal extending from (0.0, 0) to (1.0, 90). We evaluate the probability to obtain this configuration by chance.

First, we consider the case in which both aspect ratios and angles are randomly drawn from uniform distributions. Under this assumption, the desired probabilities can be obtained analytically: the diagonal splits the parameter space in two parts of equal area. Therefore, the probability for any single point to lie above or below the diagonal is 0.5, and the outcome of multiple draws obeys the binomial distribution with probability for a positive outcome equal to 0.5. If we consider all 32 data points (including the ones that did not survive our quality cuts), then we have 2/32 points above the diagonal. The probability to obtain the observed outcome or one which is *even more biased* towards points below the diagonal is the sum of the probabilities to obtain 0/32, 1/32 or 2/32 points above the diagonal:

$$P(\#\text{ above diagonal} \leq 2) = \sum_{i=0}^{2} \binom{32}{i} 0.5^i 0.5^{32-i} = 1.2 \times 10^{-7}. \tag{16}$$

If we consider only the 24 data points that survived our quality cuts, then we have 1/24 points above the diagonal, and the associated probability to have obtained such a result by chance is

$$P(\#\text{ above diagonal} \leq 1) = \sum_{i=0}^{1} \binom{24}{i} 0.5^i 0.5^{24-i} = 1.2 \times 10^{-7} \tag{17}$$

with the result being numerically approximately equal as in the previous case. This configuration is extremely unlikely to have been obtained by chance from a uniformly distributed parameter space.

Next, we consider the case in which the aspect ratio distribution in nature is identical to the observed aspect ratio distribution, but angles are randomly drawn from a uniform distribution. For each observed aspect ratio, we randomly select an angle λ, and we calculate the probability that the number of points below the diagonal is ≤ 2 for the 32 data points and ≤ 1 for the 24 data points surviving

the cuts. We find that this probability is equal to 0.98 per cent and 1.3 per cent, respectively. Although more likely than before, this scenario also has a very small probability of occurring.

A more sophisticated version of these qualitative arguments can be made starting from characteristic limiting cases for the distribution of intrinsic cloud features (shapes and magnetic field orientations). For each such case we compute, by performing 'mock observations' along randomly selected and uniformly distributed LOS, the joint probability density function (PDF) of our two observables, the elongation q and the projected field-short ellipse axis angle λ. The results are shown in Fig. 5, overplotted with the 24 observed points that survive the λ dispersion cut described in Section 2. The parameters of the intrinsic shape and field orientation distributions that lead to each PDF are given in Table 2. These parameters are as follows: in the case of the intrinsic shape distribution, the cloud ellipsoid axial ratios ($\zeta_{\max}$, $\xi_{\max}$) of the most probable shape (the values that maximize the PDF of axial ratios); and in the case of the field orientation distribution, the most probable cosine of the field orientation polar angle, $\cos\theta_{B,\max}$, and the standard deviation of the cosine of the field polar angle, $\sigma(\cos\theta_B)$. The exact functional forms of the shape and field orientation distributions used are discussed in Appendices B1 and B2.

The qualitative distribution of the data points on the q– λ plane forms a triangular shape, with the lower right part of the plot (almost circular cloud images, small angles of the magnetic field with the short ellipse axis) more populated than the upper left part of the plot (very elongated cloud images, large angles of the magnetic field with the short ellipse axis). In general, there are many fewer very elongated POS cloud ellipses than circular-looking ellipses, which qualitatively indicates oblate intrinsic shapes (since there are many more LOS that will yield a circularly looking POS ellipse for a disc-like cloud than for a cigar-like cloud). Additionally, large angles with the short ellipse axis are only encountered for almost circular cloud images (giving rise to the triangular distribution of the data on the observables plane), which qualitatively hints to an orientation of the magnetic field at small angles with the short cloud axis (so that when the cloud is viewed edge-on, the observations yield an elongated POS ellipse and a small POS field angle with the short ellipse axis, cf. Fig. 1, while when viewed face-on the cloud looks circular and a larger variety of angles of the POS field with the short ellipse axis are possible, cf. Fig. 2).

The different PDFs plotted in Fig. 5 demonstrate how the behaviour of the PDF of the observables responds to changes in the underlying distributions of shapes and field orientation. For oblate shapes, the contours of the joint PDF for λ and q for different field orientations are shown in panels (a)–(d). As expected, when the field is oriented parallel to the short cloud axis, the λ– q PDF acquires a roughly triangular shape preferentially populating the high-q low-λ corner (panel a), while for a field oriented perpendicular to the short cloud axis the PDF is also roughly triangular, however now preferentially populating the high-q high-λ corner (panel b). For the intermediate situation of a field oriented at 45° from the short

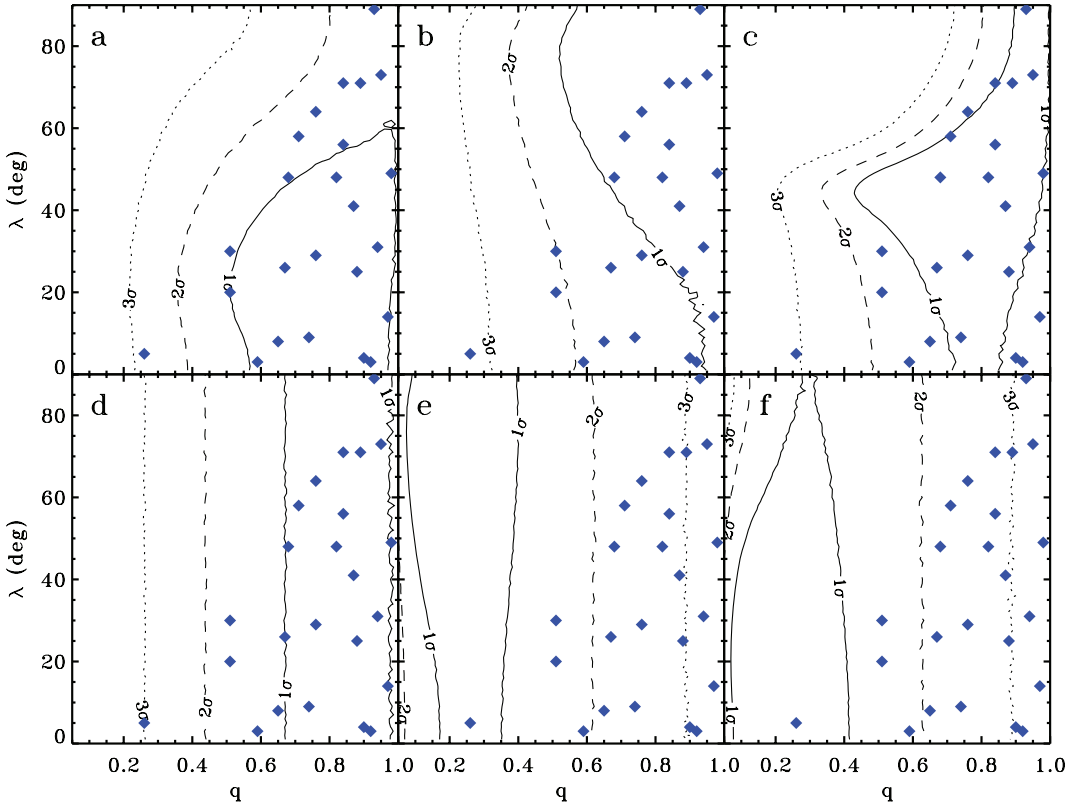

Figure 5. Contour plots of the joint PDF of the observables q and λ obtained by convolving different intrinsic distributions of cloud shapes and magnetic field orientations with random LOS. The solid, dashed and dotted lines correspond to the 1, 2 and 3σ contours, respectively. The blue data points correspond to our 24 data points surviving the quality cuts. Panel (a): oblate clouds, magnetic field preferentially oriented parallel to short cloud axis; panel (b): oblate clouds, magnetic field preferentially oriented parallel to the long cloud axis; panel (c): oblate clouds, magnetic field preferentially oriented at a 45° angle with the short cloud axis; panel (d): oblate clouds, uniformly distributed magnetic field orientations; panel (e): prolate clouds, magnetic field preferentially oriented parallel to long cloud axis; panel (f): prolate clouds, magnetic field preferentially oriented parallel to short cloud axis. The parameters of the intrinsic distributions resulting in each PDF are given in Table 2.

Table 2. Parameters of the intrinsic distributions giving rise to the PDF in each panel of Fig. 5.

Fig. 5 panels	$\zeta_{\max}$	$\xi_{\max}$	$\cos\theta_{B\max}$	$\sigma\ (\cos\theta_B)$	Qualitative behaviour
a	0.999	0.58	0.91	0.21	Oblate, B ∥ short axis
b	0.999	0.53	0.19	0.19	Oblate, B ⊥ short axis
c	0.999	0.62	0.70	0.04	Oblate, B at 45° with short axis
d	1.00	0.62	uniform in $\cos\theta_B$		Oblate, B random
e	0.29	0.08	0.19	0.19	Prolate, B⊥ short axis
f	0.29	0.08	0.91	0.16	Prolate, B∥ short axis

cloud axis, the PDF forms a 'spike' at the mid-q mid-λ part of the plot (panel c). Finally, for a random distribution of field orientations (panel d), the contours are parallel to the λ axis, with low q values preferred. PDFs resulting from prolate intrinsic cloud shapes are shown in panels (e) and (f), with panel (e) corresponding to a magnetic field oriented along the long axis (filamentary clouds formed along the magnetic field), and panel (e) corresponding to a magnetic field oriented along the short axis (filamentary clouds perpendicular to the magnetic field). In both cases, low values of q are preferred (a situation not seen in the data). The PDF of panel (e) preferentially populates the high-λ part of the plane, while the PDF of panel (f) preferentially populates the low-λ region.

We can therefore see that there is enough qualitative and quantitative variation between these PDFs so that, with a sufficiently large data set, the effect of the random orientation angles can be overcome and we can draw conclusions regarding the underlying distributions of cloud shapes and magnetic field orientations in nature.

In order to determine which such intrinsic distributions of cloud parameters fit our data best, we bin the λ–q parameter space in 5×5 bins. For each bin, we count the number of observed data points that fall within the bin limits. We parametrize the intrinsic shapes distribution as described in Appendix B1, using a bi-parametric joint distribution in ζ and ξ of non-zero spread, uniquely defined by the values of ζ and ξ where the probability density becomes maximum, $\zeta_{\max}$ and $\xi_{\max}$. We parametrize the intrinsic distribution of magnetic fields orientations as described in Appendix B2, using a bi-parametric distribution[3] in $\cos\theta_B$, uniquely defined by the value of $\cos\theta_B$ where the probability density becomes maximum, $\cos\theta_{B\max}$, and the standard deviation of the distribution, $\sigma(\cos\theta_B)$. Note that we wish to know the distribution of $\cos\theta_B$ rather than that of θ_B, since the quantity of interest is the fraction of LOS per solid angle in any given direction θ_B, which is expressed by $\cos\theta_B$ (see also discussion in Appendix B). Assuming uniformly distributed LOS, we determine the joint PDF for q, λ, and the expected counts for 24 observations in each bin, as well as the spread in the expected counts. We perform a weighted least-squares analysis to find the best-fitting parameters $\zeta_{\max}$, $\xi_{\max}$, $\cos\theta_{B\max}$, $\sigma(\cos\theta_B)$, using the inverse square of the spread in the expected counts as our weight. The details of this statistical analysis are discussed in Appendix B. Because of the non-linearity of the problem, there are no applicable analytic solutions to the minimization of the weighted sum of squared residuals. For this reason, we have used a well-tested, Monte Carlo-based approach, the 'Simulated Annealing' algorithm (Corana et al. 1987), to sample the parameter space and identify the location of the absolute minimum of the weighted sum of squared residuals.

[3]Since a likelihood analysis of the shapes alone (see discussion in Appendix B1) indicates that the distribution of cloud shapes is strongly peaked on the $\zeta = 1$ axis, implying that the long and middle axes of the cloud ellipsoid are very close to being equal, the ϕ_B angles are physically degenerate, and the only quantity of interest determining the orientation of the magnetic field is the angle with the shortest axis of the cloud ellipsoid, θ_B.

4 RESULTS

The results of our weighted least-squares analysis are shown in Fig. 6. The upper panel shows contours of weighted squared residuals, $S_{\rm weighted}$, as defined in Appendix B, on the $\zeta_{\max}$–$\xi_{\max}$ plane, with $\cos\theta_{B\max}$ and $\sigma(\cos\theta_B)$ fixed at their best-fitting values. The lower panel shows contours of $S_{\rm weighted}$ on the $\cos\theta_{B,\max}$–$\sigma(\cos\theta_B)$ plane, with $\zeta_{\max}$ and $\xi_{\max}$ fixed at their best-fitting values. The allowable values of $\sigma(\cos\theta_B)$ vary between 0 (δ-function of B-field orientations) and 0.289 (uniform distribution of B-field orientations with all orientations equally probable; see Appendix B). The colour scale corresponds to values of $S_{\rm weighted}$ from 9.7 to 25, with the contours spaced by factors of 1.1 (so the suppressed z-axis in this plot which is visualized by the contours is in logarithmic scale). The location of the minimum is indicated in each case by the white point within the back region. The outermost contour corresponds to the $S_{\rm weighted}$ value that is typically yielded by 24 observations drawn from the best-fitting intrinsic distributions due to random fluctuations, as calibrated by Monte Carlo simulations.

As expected from the qualitative arguments outlined above, oblate cloud shapes are preferred. In the case of the magnetic field orientation, there is a well-defined broad minimum in the weighted least-squares analysis, corresponding to a clear preference for a small angle from the short cloud ellipsoid axis and a moderate spread of angle about that. However, given the small number of data, the power of the test to reject models is limited, and a large fraction of the $\cos\theta_{B\max}$–$\sigma(\cos\theta_B)$ plane (excluding, however, distributions strongly peaked at large angles from the shortest cloud axis) could be consistent with the presently available data.

The best-fitting values of the parameters are shown in the first line of Table 2, and the resulting PDF of our observables, q and λ, is shown in panel (a) of Fig. 5. The best-fitting distribution of intrinsic shapes (axial ratios of the model cloud ellipsoids) and magnetic field orientation angles are shown in the upper and lower panels of Fig. 7, respectively. The most probable shape is a moderately thick oblate disc. The best-fitting shapes distribution is very strongly peaked close to $\zeta \approx 1.0$ (so clouds are likely to have very small degrees of triaxiality). On the other hand, the distribution is very spread out in ξ, implying that many different disc thicknesses are possible. Although the most probable shape is a relatively thick disc, this does not mean that all clouds are thick discs. Much thinner discs [closer to (ζ, ξ)=(1,0)], as well as very thick clouds [closer to $(\zeta, \xi) = (1, 1)$, labelled 'sphere' on the $p(\zeta, \xi) = 0$ plane], are

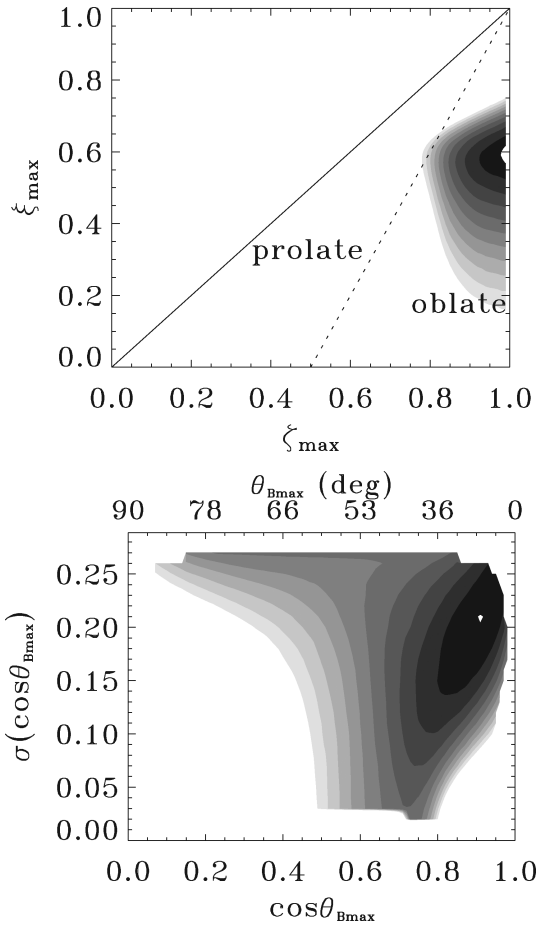

Figure 6. Contours of the weighted sum of squared residuals, $S_{\rm weighted}$, for the $(\zeta_{\rm max}, \xi_{\rm max})$ parameters (upper panel) and the $[\cos\theta_{B,\rm max}, \sigma(\cos\theta_B)]$ parameters (lower panel). The upper axis in the lower panel shows the most-probable orientation in degrees from the short cloud ellipsoid axis, corresponding to the value of $\cos\theta_{B,\rm max}$ shown in the lower axis. The two parameters *not shown* in each plot are kept fixed at their least-squares values. The colour scale corresponds to values of $S_{\rm weighted}$ from 9.7 to 25, with the contours spaced by factors of 1.1 (so the suppressed z-axis in this plot which is visualized by the contours is in logarithmic scale). The minimum is indicated in each case by the white point within the back region. The final contour corresponds to the $S_{\rm weighted}$ value that it typically yielded by 24 observations drawn from the best-fitting intrinsic distributions due to random fluctuations, as calibrated by Monte Carlo simulations. The solid line in the upper panel separates the domain of allowed values ($\zeta_0 \geq \xi_0$) from the rest of the plane, while the dotted line separates mostly oblate [$\zeta_{\rm max} \geq 0.5(1+\xi_{\rm max})$] from mostly prolate [$\zeta_{\rm max} < 0.5(1+\xi_{\rm max})$] most-probable ellipsoids.

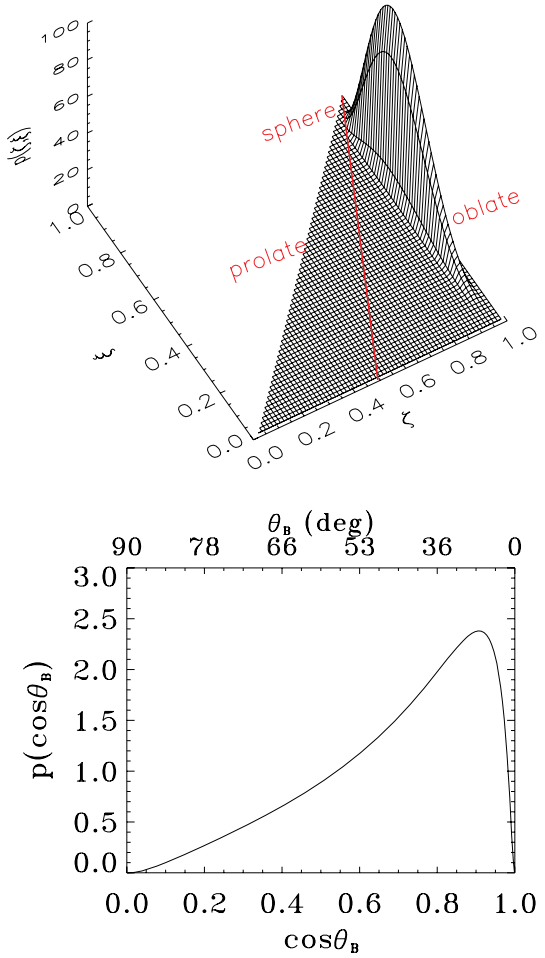

Figure 7. Best-fitting intrinsic distributions of cloud axial ratios (upper panel) and of magnetic field orientation angles (lower panel). In the upper panel, the red line extending from $(\zeta, \xi) = (1, 1)$ to $(\zeta, \xi) = (0.5, 0)$ separates the $p(\zeta, \xi) = 0$ plane in two sections: ellipsoids with axis ratios to the left of this line are mostly prolate, and ellipsoids to the right of the line are mostly oblate. Infinitesimally thin discs have $(\zeta, \xi) = (1, 0)$; infinitesimally thin cigars have $(\zeta, \xi) = (0, 0)$ and perfect spheres have $(\zeta, \xi) = (1, 1)$.

also frequently encountered although not equally common in this distribution.

The most probable magnetic field orientation has a small offset ($\theta_{B0} \sim 24^\circ$) from the short ellipsoid axis, and the standard deviation in $\cos\theta_B$ of ~0.21. These results are robust against the removal of any outliers from our data set of 24 observations. For example, when repeating the analysis without our most elongated cloud (DR 21), the best-fitting parameters of the shape distribution change from $(\zeta_{\rm max}, \xi_{\rm max}) = (0.999, 0.58)$ to $(\zeta_{\rm max}, \xi_{\rm max}) = (0.986, 0.64)$, while the best-fitting parameters of the B-field orientations distribution change from $[\cos\theta_{V\rm max}, \sigma(\cos\theta_B)] = (0.91, 0.21)$ to $[\cos\theta_{V\rm max}, \sigma(\cos\theta_B)] = (0.86, 0.19)$ – a change smaller than 10 per cent in any one of the parameters, while the qualitative behaviour of the underlying distributions remains unchanged. This result is not surprising: in the upper left panel of Fig. 2 DR 21 is outside the 2σ contour of the best-fitting joint PDF for q and λ, and barely within the 3σ contour.

As indicated by the broadness of the minimum of $S_{\rm weighted}$ as a function of our fitted parameters, the best-fitting intrinsic distributions of shapes and field orientations are not unique in their ability to yield $q-\lambda$ PDFs that are acceptable representations of the data used in this analysis. However, both the qualitative arguments presented in Section 3.2 and the location of the minimum of $S_{\rm weighted}$ indicate that oblate shapes and mean magnetic field orientations with small deviations from the shortest axis of the cloud are preferred.

5 DISCUSSION

In this paper, we have presented a new method for quantitatively assessing the intrinsic shapes and the orientations of the mean, ordered component of the magnetic field of molecular clouds, using observations of the apparent aspect ratios q and angles λ between the apparent mean magnetic field and the apparent short axis of

the POS cloud images. Under the assumption that the LOS towards the observed clouds has random orientations with respect to the principal cloud axes, we have explored different statistical methods to evaluate the consistency of various models for the intrinsic shapes and intrinsic magnetic field orientations of clouds with our data. We have used data from 24 molecular clouds obtained through 350 μm observations with the Hertz polarimeter (Dotson et al. 2009).

Based on our data sample we can exclude certain simple scenarios with high confidence. A scenario in which both cloud aspect ratios and magnetic field orientation angles are randomly drawn from uniform distributions can be excluded at the 10^{-7} level. A less restrictive scenario, in which the distribution of cloud aspect ratios is identical to the one observed in the data but magnetic field orientations are drawn randomly from a uniform distribution, is also excluded at the 10^{-2} level.

In order to examine more general cases, we have employed a weighted least-squares analysis to derive the best-fitting intrinsic shapes and intrinsic magnetic field orientations of the clouds in our sample. We have found that the most probable intrinsic shape is a thick (short-to-long axis ratio $\sim$0.6) oblate disc with a negligible degree of triaxiality (middle to long axis ratio $\sim$0.99); the best-fitting distribution of cloud thicknesses was found to be broad, so both thin and thick clouds are frequently encountered under this distribution. The most likely orientation of the magnetic field is close to the shortest axis of the cloud ($\sim$24° offset towards the middle/long axis). The best-fitting distribution of magnetic field orientations is clearly peaked around this value, but also features long tails. We have found that the best-fitting distribution of shapes and orientations, when convolved with a random LOS distribution, yields a distribution of observables which is in good agreement with the data. Our results are robust against the removal of any single point in our data set (for example, if we repeat the analysis without our most elongated cloud, DR 21, the change in our best-fitting parameters is smaller than 10 per cent).

These results are in agreement with the qualitative trend seen in the data, where clouds with small apparent aspect ratio (apparently elongated clouds) have small angles between the mean projected magnetic field direction and the short axis of the cloud ellipse; clouds which are apparently circular on the other hand can have a large range of angles between mean magnetic field and short axis. Finally, apparently elongated clouds with large angles between mean field direction and short cloud axis are not seen in the data. As far as the distribution of apparent cloud shapes is concerned, more clouds are seen to have large aspect ratios (and are thus close to circular) while only a few clouds are apparently very elongated.

Indeed, clouds which are intrinsically discs with the magnetic field direction close to that of the shortest cloud axis would exhibit similar properties when viewed through a random LOS. More LOSs yield a disc seen almost face-on rather than edge-on, so most clouds would look almost circular and only a few would appear significantly elongated (in contrast to prolate clouds, most of which would appear elongated, and randomly shaped clouds, which would show no preference in apparent aspect ratio). In addition, when clouds are seen almost edge-on and appear elongated, the magnetic field will be aligned with the short axis of the projection of the cloud on the POS. In contrast, when clouds are seen face-on, the magnetic field projection could from any angle with respect to the short and long axes of the cloud ellipse, which in reality are, in this case, projections of the cloud ellipsoid middle and long axes.

Despite the preference of the data for such a scenario, and the clear potential of this test for discriminating between scenarios for intrinsic magnetic field orientations in molecular clouds and between theories for molecular cloud dynamics, we have shown quantitatively that a larger number of observations are needed for the test to conclusively reject alternative configurations. With the present, limited number of observed clouds, the distributions of LOS, magnetic field orientations and shapes are still sparsely sampled, and as a result random fluctuations in this sampling allow for a large number of parameters to yield acceptable representations of the observed q and λ. However, our results explicitly demonstrate that there is no *intrinsic* degeneracy in the distributions of q and λ yielded by different classes of cloud shapes and magnetic field orientations in nature, so a large number of q, λ observations should allow conclusive tests of different underlying distributions.

Our analysis has the advantage that it is not a priori tied to any theory or prediction regarding the dynamical processes in molecular clouds, but rather allows the data to pick freely the part of the shapes/orientations parameter space that best fits the observations. We have additionally tested that the location of the best-fitting $\zeta_{\max}$, $\xi_{\max}$, $\cos\theta_{B\max}$, and the spread of the orientations distribution are robust with respect to changes in the assumed functional form or the details of the analysis (for example, performing a joint analysis for the shapes and orientations, or performing an analysis for the shapes alone). Finally, observational uncertainties in the measured quantities are expected to have a limited effect in our analysis, as the binning of the (q, λ) parameter space involves bins that are typically of the same order as or wider than such uncertainties.

The *apparent* orientation of the magnetic field in molecular clouds and cloud cores has been studied in the past by various authors. Kane et al. (1993), using 1.3 mm polarization measurements, claimed a strong preference for alignment of the polarized emission with the structure in deconvolved *IRAS* maps. Glenn, Walker & Young (1999) used a sample of seven elongated cloud cores selected to have a polarization detection greater than 3σ at either 800 μm or 1.3 mm. They found that the orientation of the apparent magnetic field was random with respect to the apparent cloud axes. Vallée & Bastien (1999), using 760 μm observations, found the apparent magnetic field direction in molecular cloud cores (intensity peaks within clouds) to be parallel to the apparent minor axis in three out 10 cases. These studies all focused on polarization vectors measured at intensity peaks, contrary to our own survey, where polarization is extensively mapped throughout the clouds in our sample. The intrinsic *shapes* of molecular clouds were discussed by Kerton et al. (2003). Based on the Five College Radio Astronomy Observatory Outer Galaxy Survey in CO emission, they studied a sample of 15 000 clouds. They concluded that the intrinsic shapes of these objects are best described as intermediate between near-oblate and near-prolate ellipsoids.

Our results have important implications concerning the dynamical importance of magnetic fields in molecular clouds. If magnetic fields are dynamically unimportant compared to turbulent motions, the fields are expected to be carried around with turbulent eddies in the cloud, and show little correlation with the principal cloud axes. However, our data show clear indications that such a correlation exists. Our results are also unfavourable for the scenario of helical magnetic fields threading prolate clouds. Not only are the predicted 90° flips in the polarization vectors not observed (Dotson et al. 2009), but clouds in our sample are found to be oblate, rather than prolate. This result is also consistent with the argument against prolate cloud *cores*, which are also predicted in this scenario (Fiege & Pudritz 2000c), but are not observed in nature (Jones, Basu & Dubinski 2001; Jones & Basu 2002; Tassis 2007).

If, on the other hand, magnetic fields are dynamically important, cloud shapes should be close to oblate discs, and the magnetic field

should be closely aligned with the short axis of the cloud ellipsoid. This scenario seems to be the one which yields the best agreement with our data. Intrinsic cloud shapes are indeed very strongly peaked around oblate discs. The best-fitting magnetic field orientation is close to the shortest cloud ellipsoid axis, with small offsets towards the middle/long axes. However, more data are required before a more robust quantitative statement can be made with regard to both the details of the best-fitting underlying magnetic fields orientation distribution and the confidence with which alternative scenarios can be rejected.

In addition to support from our statistical treatment, this picture is also consistent with observations of individual well-studied systems where projection effects are minimal. In these cases, the hourglass morphology of the magnetic field, characteristic of dynamically important magnetic fields, is seen in very different scales, from clouds to dense cores (e.g. Schleuning 1998, in the case of the cloud OMC-1; Girart, Rao & Marrone 2006, in the case of protostellar core NGC 1333; Lai et al. 2002, in the case of massive core NGC 2024).

We conclude by stressing that although our analysis has yielded best-fitting distributions that seem to *prefer* this portion of the parameter space, the rejection power of our test, especially in the case of magnetic field orientations, is limited given the present sample size. Stronger constraints on the intrinsic statistics of magnetic field orientations in nature will require polarimetry observations in a larger number of clouds.

ACKNOWLEDGMENTS

KT thanks Shantanu Basu and Vasiliki Pavlidou for useful discussions, and Nick Scoville, Paul Goldsmith and Telemachos Mouschovias for feedback on the manuscript. We thank the referee, Carl Heiles, for insightful comments which helped us improve the manuscript. KT acknowledges support by NSF grants AST 02-06216 and AST02-39759, by the NASA Theoretical Astrophysics Program grant NNG04G178G and by the Kavli Institute for Cosmological Physics at the University of Chicago through grants NSF PHY-0114422 and NSF PHY-0551142 and an endowment from the Kavli Foundation and its founder Fred Kavli. JEV acknowledges support from NSF AST 05-40882 through the Caltech Submillimeter Observatory. RH and LK acknowledge support from NSF grant AST 0505124. Part of this work was carried out at the Jet Propulsion Laboratory, California Institute of Technology, under a contract with the National Aeronautics and Space Administration.

REFERENCES

Ballesteros-Paredes J., Vázquez-Semadeni E., Scalo J., 1999, ApJ, 515, 286
Basu S., 2000, ApJ, 540, L103
Binney J., 1985, MNRAS, 212, 767
Bethell T. J., Chepurnov A., Lazarian A., Kim J., 2007, ApJ, 663, 1055
Burkert A., Hartmann L., 2004, ApJ, 616, 288
Corana A., Marchesi M., Martini C., Ridella S., 1987, ACM Trans. Math. Soft., 13, 262
Curran R. L., Chrysostomou A., 2007, MNRAS, 382, 699
Draine B. T., Lee H. M., 1985, ApJ, 290, 211
Dotson J. L., Davidson J., Dowell C. D., Schleuning D. A., Hildebrand R. H., 2000, ApJS, 128, 335
Dotson J. L., Davidson J. A., Dowell C. D., Hildebrand R. H., Kirby L., Vaillancourt J. E., 2009, ApJS, submitted
Dowell C. D., Hildebrand R. H., Schleuning D. A., Vaillancourt J. E., Dotson J. L., Novak G., Renbarger T., Houde M., 1998, ApJ, 504, 588
Fiege J. D., Pudritz R. E., 2000a, MNRAS, 311, 85
Fiege J. D., Pudritz R. E., 2000b, ApJ, 544, 830
Fiege J. D., Pudritz R. E., 2000c, ApJ, 534, 291
Gammie C. F., Lin Y.-T., Stone J. M., Ostriker E. C., 2003, ApJ, 592, 203
Girart J. M., Rao R., Marrone D. P., 2006, Sci, 313, 812
Glenn J., Walker C. K., Young E. T., 1999, ApJ, 511, 812
Hartmann L., Burkert A., 2007, ApJ, 654, 988
Hildebrand R. H., Davidson J. A., Dotson J. L., Dowell C. D., Novak G., Vaillancourt J. E., 2000, PASP, 112, 1215
Hoang T., Lazarian A., 2008, MNRAS, 388, 117
Jones C. E., Basu S., 2002, ApJ, 569, 280
Jones C. E., Basu S., Dubinski J., 2001, ApJ, 551, 387
Kane B. D., Clemens D. P., Barvainis R., Leach R. W., 1993, ApJ, 411, 708
Kerton C. R., Brunt C. M., Jones C. E., Basu S., 2003, A&A, 411, 149
Lai S.-P., Crutcher R. M., Girart J. M., Rao R., 2002, ApJ, 566, 925
Lazarian A., 2003, J. Quant. Spectrosc. Radiative Transfer, 79, 881
Lazarian A., 2007, J. Quant. Spectrosc. Radiative Transfer, 106, 225
Mouschovias T. C., 1978, IAU Colloq. 52: Protostars and Planets, 209
Naghizadeh-Khouei J., Clarke D., 1993, A&A, 274, 968
Schleuning D. A., 1998, ApJ, 493, 811
Schleuning D. A., Dowell C. D., Hildebrand R. H., Platt S. R., 1997, PASP, 109, 307
Tassis K., 2007, MNRAS, 379, L50
Vaillancourt J. E., 2006, PASP, 118, 1340
Vallée J. P., Bastien P., 1999, ApJ, 526, 819

APPENDIX A: PROJECTION EFFECTS

Let us consider a triaxial ellipsoid model molecular cloud of semi-axes $a \geq b \geq c$, and a *native* system of coordinates (x, y, z) centred on the cloud and aligned with its axes. The triaxial ellipsoid *surface* in this system obeys

$$\frac{x^2}{a^2} + \frac{y^2}{b^2} + \frac{z^2}{c^2} = 1\,. \tag{A1}$$

The x-, y- and z-axes are thus oriented along the longest, middle and shortest ellipsoid axes, respectively. Let us additionally define a second, *observation* system of coordinates, (x', y', z'). In this system, the LOS is along the z' axis, and consequently the x'–y' plane is the POS. The x' axis is in the x–y plane, which implies that $x' \perp z$. The y' axis thus represents the projection on to the POS of the z-axis, and consequently of the shortest axis of the cloud ellipsoid. The orientation between the native and observation systems of coordinates is given by the angles θ and ϕ between the z and z' axes and the x and x' axes, respectively (see Fig. 4).

When observed, the image of the molecular cloud appears on the POS as an ellipse. The properties of this projected, observed ellipse can be calculated from the properties of the cloud ellipsoid and the orientation of the observer's LOS[4] (Binney 1985). We define the axial ratios as $\zeta = b/a$ and $\xi = c/a$, so $1 \geq \zeta \geq \xi$. Then, the POS isophotes of an ellipsoid molecular cloud, the shape of which

[4]Note that the projection we are referring to here is not a 'cut' of the cloud ellipsoid along some plane, but rather the surface brightness along the observer's LOS (and hence it represents an integral of the cloud density along the LOS).

is described by equation (A1), will be coaxial ellipses of aspect ratio

$$1 \geq q(\theta, \phi, \zeta, \xi) = \sqrt{\frac{A + C - \sqrt{(A-C)^2 + B^2}}{A + C + \sqrt{(A-C)^2 + B^2}}} \tag{A2}$$

where

$$A \equiv \frac{\cos^2\theta}{\xi^2}\left(\sin^2\phi + \frac{\cos^2\phi}{\zeta^2}\right) + \frac{\sin^2\theta}{\zeta^2}\,, \tag{A3}$$

$$B \equiv \cos\theta \sin 2\phi \left(1 - \frac{1}{\zeta^2}\right)\frac{1}{\xi^2}\,, \tag{A4}$$

$$C \equiv \left(\frac{\sin^2\phi}{\zeta^2} + \cos^2\phi\right)\frac{1}{\xi^2}\,. \tag{A5}$$

The orientation of the axes of the POS cloud ellipse with respect to the POS axes (x' and y') is given by the angle ψ, defined as

$$\psi = \frac{1}{2}\arctan\left(\frac{B}{A-C}\right)\,. \tag{A6}$$

In equation (A6), ψ can be the angle between either the minor or the major axis of the POS ellipse with the y' axis (the sum of the two angles is always equal to 90°, and ψ, which can take values between 0 and 45°, is always the smaller of the two). Which one of the two angles is represented by ψ in each case is determined by the sign of the quantity

$$u = (A - C)\cos 2\psi + B \sin 2\psi\,. \tag{A7}$$

If $u \leq 0$, ψ represents the angle between the minor ellipse axis and y'. If $u > 0$, ψ represents the angle between the major axis and y'. The sign of ψ indicates the quadrant in which the relevant axis (major or minor, depending on the sign of u) resides. If $\psi \leq 0$ the relevant axis is located in the first/third quadrant, while if $\psi > 0$ the relevant axis is located in the second/fourth quadrant.

Additionally, let us consider that the cloud is threaded by a large-scale ordered magnetic field $\boldsymbol{B}$, which has some orientation with respect to the cloud principal axes characterized by a set of angles (θ_B, ϕ_B); here, θ_B is the angle of the magnetic field with the shortest cloud axis z and ϕ_B is the angle of its projection on to the plane (x, y) defined by the directions of the middle and longest axes (see Fig. 4). We are interested in the orientation of the POS projection of $\boldsymbol{B}$, since this is what can be measured through polarimetry observations. The components of $\boldsymbol{B}$ in the (x, y, z) coordinate system are

$$\boldsymbol{B} = B\begin{pmatrix}\sin\theta_B\cos\phi_B\\ \sin\theta_B\sin\phi_B\\ \cos\theta_B\end{pmatrix}\,. \tag{A8}$$

Performing the rotation to the (x', y', z') coordinate system we find that the x' and y' components of $\boldsymbol{B}$ (the POS components) are

$$B_{x'} = B\,[-\sin\phi\sin\theta_B\cos\phi_B + \cos\phi\sin\theta_B\sin\phi_B] \tag{A9}$$

and

$$B_{y'} = B\,[-\cos\phi\cos\theta\sin\theta_B\cos\phi_B - \sin\phi\cos\theta\sin\theta_B\sin\phi_B + \sin\theta\cos\theta_B]\,. \tag{A10}$$

The angle ω between the POS projection of $\boldsymbol{B}$ and the POS projection of the shortest cloud axis (the y' axis) is given by

$$\tan\omega = \frac{\sin\phi\sin\theta_B\cos\phi_B - \cos\phi\sin\theta_B\sin\phi_B}{\cos\theta\sin\theta_B(\cos\phi\cos\phi_B + \sin\phi\sin\phi_B) - \sin\theta\cos\theta_B}\,. \tag{A11}$$

Note that, contrary to ψ, the angle ω is, by definition, positive in the first–third quadrant, and negative in the second–fourth quadrant, where x' and y' have opposite signs.

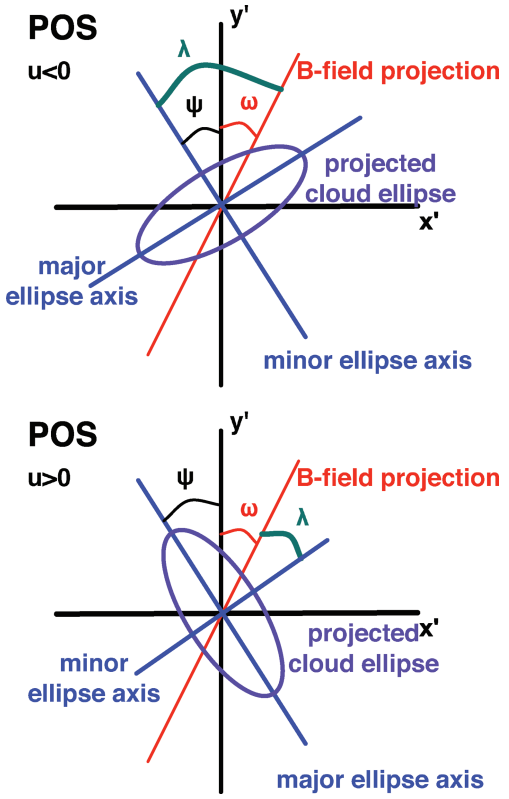

Figure A1. POS angles between the POS projection of the magnetic field (red line), the POS projection of the shortest cloud ellipsoid axis (the y' axis) and the projected cloud ellipse axes (blue lines). Upper panel: $u < 0$ (ψ represents the angle between y' and the *minor* ellipse axis). Lower panel: $u > 0$ (ψ represents the angle between y' and the *major* ellipse axis). The magnitude of the angle λ is the observable angle between the POS cloud ellipse minor axis and the POS projection of the magnetic field. In this case, ψ and ω are both positive, and $|\psi + \omega| < 90°$.

The angle that can be determined observationally, however, is not ω, but rather the magnitude of the angle λ between the POS projection of $\boldsymbol{B}$ and one axis (for definiteness we will use the minor axis) of the POS cloud ellipse. The relation between λ, ω and ψ is different, depending on the value of u (see Fig. A1):

$$\lambda = \begin{cases} 90° - \left|90° - |\psi + \omega|\right|\,, & u \leq 0 \\ \left|90° - |\psi + \omega|\right|\,, & u > 0 \end{cases}\,. \tag{A12}$$

We have therefore shown that the two observable quantities q and λ can be calculated using the formalism described above, provided that we know:

(a) the intrinsic shape of the cloud ellipsoid (i.e. its axial ratios ζ and ξ);

(b) the orientation of the ordered magnetic field with respect to the native coordinate system (i.e. the angles θ_B and ϕ_B) and

(c) the orientation of the LOS with respect to the native coordinate system (i.e. the angles θ and ϕ).

Note that the angles θ_B and ϕ_B only enter the calculation of λ, while q is not dependent on them. Because the LOS is random, λ is not fixed, even if the true magnetic field direction is fixed with respect to the true cloud ellipsoid axes, *and* all molecular clouds have the exact same intrinsic shape (see e.g. Basu 2000). Rather, there is a distribution of such angles, which can be calculated analytically, given our hypothesis for the orientation of the true mean magnetic

field in the clouds, as well as some knowledge of the distribution of intrinsic cloud shapes in nature.

APPENDIX B: STATISTICAL ANALYSIS

In this work, we use our set of observations of the aspect ratio q of the POS cloud ellipse and the magnitude of the angle λ between the POS projection of the magnetic field and the minor axis of the POS cloud ellipse to constrain the intrinsic shapes and magnetic field orientations in molecular clouds. Unfortunately, it is not possible to derive directly the intrinsic shape and the orientation of the magnetic field in each cloud, as this would require knowledge of the LOS orientation in each case. Instead, we employ a statistical analysis, assuming that the distribution of LOS orientations is uniform with respect to all directions (same fraction of LOS per unit solid angle in all directions). In practice, this means that the distribution of $\cos\theta$ is uniform with values between -1 and 1, and the distribution of ϕ is also uniform with values between 0 and 2π.

Under this assumption, we will perform a weighted least-squares analysis to deduce the best-fitting PDF of our observables, q and λ, and the associated distributions of intrinsic shapes and orientations of the magnetic field with respect to the principal cloud ellipsoid axes that generate it.

Because the magnetic field orientation does not enter the calculation of q, it is also possible to use *only* the observations of q to derive the best-fitting distribution of the intrinsic molecular cloud shapes (an analysis similar to that of Tassis 2007 in the case of molecular cloud cores). The results obtained by this q-only analysis indicate that the distribution of intrinsic shapes is strongly peaked on the $\zeta = 1$ axis (largest and middle axes equal) so that all azimuthal magnetic field angles ϕ_B are physically equivalent. For this reason, we will treat the orientation angle ϕ_B as random and uniformly distributed, and we will only attempt to determine the best-fitting distribution of $\cos\theta_B$, determining the most likely deviation of the magnetic field orientation from the shortest cloud axis. Note that the relevant quantity is $\cos\theta_B$, rather than θ_B, as we are interested not only in the most probable angle, but also on the spread of such angles: one of the theoretical cases we would like to test is that where all magnetic field orientations have an equal probability of occurring. This translates to a uniform distribution of magnetic field orientations per solid angle around the cloud centre, which in turn is mathematically expressed as a uniform distribution in $\cos\theta_B$. Thus, the interpretation of a best-fitting distribution in $\cos\theta_B$ is intuitively straightforward: the standard deviation corresponding to a δ-function in preferred field orientation is $\sigma(\cos\theta_B) = 0$, while the standard deviation corresponding to a uniform orientation distribution is $\sigma(\cos\theta_B) = \sqrt{\langle(\cos\theta_B)^2\rangle - \langle\cos\theta_B\rangle^2} = \sqrt{1/3 - 1/4} = 0.289$. Moderately spread distributions will have a standard deviation in between.

Our primary statistical analysis is performed under the following assumptions.

(i) Molecular clouds can be described as triaxial ellipsoids of the form of equation (A1).

(ii) The axial ratios ζ and ξ of molecular cloud ellipsoids have an intrinsic distribution in nature, of the form described in Appendix B1, with two free parameters, $\zeta_{\max}$ and $\xi_{\max}$ (the ζ and ξ which maximize the distribution and correspond to the most probable shape).

(iii) ϕ_B has a uniform distribution between 0 and 2π; $\cos\theta_B$ has an intrinsic distribution of the form described in Appendix B2, with two free parameters $\cos\theta_{B,\max}$, and $\sigma(\cos\theta_B)$ (corresponding to the most probable orientation and the standard deviation of the distribution of $\cos\theta_B$).

(iv) The orientation angles of the LOS with respect to the native coordinate system, θ and ϕ, are random and all equally probable: the distribution of $\cos\theta$ is uniform with values between -1 and 1, and the distribution of ϕ is uniform with values between 0° and 360°.

Based on these assumptions, we calculate, for every set of distribution parameters $\zeta_{\max}$, $\xi_{\max}$, $\cos\theta_{B,\max}$ and $\sigma(\cos\theta_B)$, the expectation value of the number of observed points in each bin on the $q-\lambda$ plane, if 24 observations are performed with random LOS; we also calculate the spread of the observed number of points. We do so using the following Monte Carlo procedure.

(i) We randomly draw a pair of ζ, ξ and a $\cos\theta_B$ from their respective distributions, and a ϕ_B from a uniform distribution between 0 and 2π.

(ii) We randomly draw a LOS orientation, by drawing a pair of θ, ϕ from a uniform probability distribution [equal probability for any value of $\cos\theta$ or ϕ in the intervals (0, 1) and (0, 2π), respectively].

(iii) We use the values of ζ, ξ, θ and ϕ to calculate q, u and ψ through equations (A2)–(A7).

(iv) We use the values of θ_B, ϕ_B, θ and ϕ to calculate ω through equation (A11).

(v) We use the values of ω, ψ and u to calculate λ through equation (A12).

(vi) We repeat Steps (i)–(v) 24 times (as many as our observed clouds). For every bin in the $q-\lambda$ plane, we calculate the number of observations that fall within its limits.

(vii) We repeat Step (vi) 10 000 times. Using the 10 000 mock sets of 24 observations, we calculate for each bin i the mean number of observations, $\langle N_i\rangle$ (which has to be $0 \le \langle N_i\rangle \le 24$), and the sample variance of N_i, $\sigma^2_{Ni} = \langle N_i^2\rangle - \langle N_i\rangle^2$. Because we only use 10 000 mock observations and we use the inverse of σ^2_{Ni} as a weight in our least-squares analysis, for the cases wherein our 10 000 trials we obtain $\sigma^2_{Ni} = 0$ we use instead a floor value of $\sigma^2_{Ni} = 10^{-4}$.

We finally obtain the best-fitting set of parameters $\zeta_{\max}$, $\xi_{\max}$, $\cos\theta_{B,\max}$, and $\sigma(\cos\theta_B)$ by minimizing the weighted squared residuals function:

$$S_{\text{weighted}}(\zeta_{\max}, \xi_{\max}, \cos\theta_{B,\max}, \sigma(\cos\theta_B)) = \sum_{i=1}^{5\times5} \frac{N_{\text{data,i}} - \langle N_i\rangle}{\sigma^2_{N_i}} . \tag{B1}$$

B1 Modified lognormal distribution of intrinsic cloud shapes

We wish to use a distribution of finite width in each of the ζ, ξ axes which is, however, smooth and has a relatively sharp maximum. Such a distribution is a modified lognormal, which we construct in the following way: we first seek an appropriate minimal transformation which will transform the domain of ζ and ξ from (0, 1) to $(-\infty, \infty)$; we then take the transformed variable to follow a Gaussian distribution.

An appropriate transformation is $\zeta \to x$ and $\xi \to y$ where

$$x = \ln\frac{\zeta}{1-\zeta} \tag{B2}$$

and

$$y = \ln\frac{\xi}{\zeta-\xi} . \tag{B3}$$

It is easy to see that

$$\lim_{\zeta\to 0} x = -\infty, \quad \lim_{\zeta\to 1} x = \infty, \quad \lim_{\xi\to 0} y = -\infty, \quad \lim_{\xi\to 1} y = \infty.$$

If then the joint probability distribution function (PDF of x and y is

$$p(x, y) = \frac{1}{2\pi\sigma_x\sigma_y} \exp\left[-\frac{(x-x_0)^2}{2\sigma_x^2}\right] \exp\left[-\frac{(y-y_0)^2}{2\sigma_y^2}\right], \quad \text{(B4)}$$

then the joint PDF of ζ and ξ will be

$$p(\zeta, \xi) = \frac{1}{2\pi\sigma_x\sigma_y} \exp\left[-\frac{\left(\ln\frac{\zeta}{1-\zeta} - x_0\right)^2}{2\sigma_x^2}\right] \times \exp\left[-\frac{\left(\ln\frac{\xi}{\zeta-\xi} - y_0\right)^2}{2\sigma_y^2}\right] \frac{1}{\xi(\zeta-\xi)(1-\zeta)}. \quad \text{(B5)}$$

This is in principle a tetra-parametric distribution with parameters x_0, y_0, σ_x and σ_y. However, to reduce the number of parameters entering the problem and the associated computation time required for the analysis, while at the same time allowing the expected amount of variation in molecular cloud shapes, we fix the value of σ_x and σ_y to 0.2 and 0.7 respectively, determined from a likelihood analysis[5] of the aspect ratios q alone.

The values $\zeta = \zeta_{\max}$ and $\xi = \xi_{\max}$ that maximize $p(\zeta, \xi)$ are given by the system of equations

$$\partial p/\partial\xi = 0 \quad \text{(B6)}$$

$$\partial p/\partial\zeta = 0 \quad \text{(B7)}$$

or, equivalently,

$$0 = \sigma_y^2\left(\ln\frac{\zeta}{1-\zeta} - x_0\right)(\zeta-\xi) - \sigma_x^2\left(\ln\frac{\xi}{\zeta-\xi} - y_0\right)(1-\zeta)\zeta + (1-2\zeta+\xi)\zeta\sigma_x^2\sigma_y^2, \quad \text{(B8)}$$

[5]For details on the methodology of this shapes-only likelihood analysis see Tassis (2007).

$$0 = \left(\ln\frac{\xi}{\zeta-\xi} - y_0\right)\frac{\zeta}{\sigma_y^2} + \zeta - 2\xi. \quad \text{(B9)}$$

With σ_x and σ_y fixed, $\zeta_{\max}$ and $\xi_{\max}$ can be used alternatively as the free parameters of $p(\zeta, \xi)$.

B2 Modified lognormal distribution of intrinsic magnetic field orientations

The distribution of $\cos\theta_B$ follows a modified lognormal similar to the one discussed in Appendix B1: let the variable w follow a Gaussian distribution with parameters w_0, σ_w, and let $\cos\theta_B$ be related to w through the transformation

$$w = \ln\frac{\cos\theta_B}{1-\cos\theta_B}. \quad \text{(B10)}$$

In this way, the PDF of $\cos\theta_B$ is

$$p(\cos\theta_B) = \frac{1}{\sqrt{2\pi}\sigma} \exp\left[-\frac{\left(\ln\frac{\cos\theta_B}{1-\cos\theta_B} - w_0\right)^2}{2\sigma_w^2}\right] \times \frac{1}{\cos\theta_B(1-\cos\theta_B)}. \quad \text{(B11)}$$

The value of $\cos\theta_B$ where $p(\cos\theta_B)$ is maximized, which we call $\cos\theta_{B\max}$, is obtained by requiring that $\mathrm{d}p/\mathrm{d}\cos\theta_B = 0$, or, equivalently, by solving the equation

$$-\ln\frac{\cos\theta_B}{1-\cos\theta_B} w_0 - \sigma_w^2 + 2\sigma_w^2\cos\theta_B = 0. \quad \text{(B12)}$$

The standard deviation of this distribution is obtained through

$$\sigma(\cos\theta_B) = \sqrt{\int_{\cos\theta_B=0}^{1} (\cos\theta_B - \langle\cos\theta_B\rangle)^2\, p(\cos\theta_B) d\cos\theta_B}, \quad \text{(B13)}$$

with

$$\langle\cos\theta_B\rangle = \int_{\cos\theta_B=0}^{1} \cos\theta_B\, p(\cos\theta_B) d\cos\theta_B. \quad \text{(B14)}$$

This is a bi-parametric distribution, with free parameters w_0 and σ_w or, equivalently, $\cos\theta_{B\max}$ and $\sigma(\cos\theta_B)$.

This paper has been typeset from a TEX/LATEX file prepared by the author.